

PHYSICS

Nonequilibrium electron and lattice dynamics of strongly correlated $\text{Bi}_2\text{Sr}_2\text{CaCu}_2\text{O}_{8+\delta}$ single crystals

Tatiana Konstantinova,^{1,2*} Jonathan D. Rameau,¹ Alexander H. Reid,³ Omadillo Abdurazakov,⁴ Lijun Wu,¹ Renkai Li,³ Xiaozhe Shen,³ Genda Gu,¹ Yuan Huang,¹ Laurenz Rettig,⁵ Isabella Avigo,⁵ Manuel Ligges,⁵ James K. Freericks,⁶ Alexander F. Kemper,⁴ Hermann A. Dürr,³ Uwe Bovensiepen,⁵ Peter D. Johnson,¹ Xijie Wang,³ Yimei Zhu^{1,2*}

The interplay between the electronic and lattice degrees of freedom in nonequilibrium states of strongly correlated systems has been debated for decades. Although progress has been made in establishing a hierarchy of electronic interactions with the use of time-resolved techniques, the role of the phonons often remains in dispute, a situation highlighting the need for tools that directly probe the lattice. We present the first combined megaelectron volt ultrafast electron diffraction and time- and angle-resolved photoemission spectroscopy study of optimally doped $\text{Bi}_2\text{Sr}_2\text{CaCu}_2\text{O}_{8+\delta}$. Quantitative analysis of the lattice and electron subsystems' dynamics provides a unified picture of nonequilibrium electron-phonon interactions in the cuprates beyond the N -temperature model. The work provides new insights on the specific phonon branches involved in the nonequilibrium heat dissipation from the high-energy Cu–O bond stretching “hot” phonons to the lowest-energy acoustic phonons with correlated atomic motion along the $\langle 110 \rangle$ crystal directions and their characteristic time scales. It reveals a highly nonthermal phonon population during the first several picoseconds after the photoexcitation. The approach, taking advantage of the distinct nature of electrons and photons as probes, is applicable for studying energy relaxation in other strongly correlated electron systems.

INTRODUCTION

Time-resolved methods (1) are useful tools for studying systems with strong correlations among charge, spin, and lattice degrees of freedom because they allow temporal separation of the many-body interactions. However, most of the experimental techniques, time- and angle-resolved photoemission spectroscopy (tr-ARPES) and pump-probe optical spectroscopy, are primarily sensitive to the electronic density of states and provide only indirect information about the lattice dynamics. Questions about how exactly the energy, transferred to the lattice, redistributes within the subsystem and on what time scales often cannot be answered with the use of the above methods.

The high- T_c cuprate superconductors are among the strongly correlated systems whose nonequilibrium lattice dynamics attract scientific attention due to their potential involvement in the pairing mechanism (2), pseudogap formation (3) and its role in relaxation of photoexcited carriers (4), and the photoinduced superconducting state (5). Recent investigations of high- T_c cuprate superconductors by tr-ARPES (4, 6–8), pump-probe reflectivity (9), and optical spectroscopy (10) show that the excited carrier dynamics display three distinct time scales (20 fs, 100 fs, and 1 to 2 ps) attributed to electron interaction with bosonic modes of electronic origin (10, 11), to strong selective or preferential coupling to a limited subset of optical phonon branches (4, 7), and to the rest of the available lattice vibrations, respectively. However, this model has not been confirmed by direct lattice measurements nor have the relevant phonon branches been unambiguously identified. The knowledge of the thermalization pathway within the lattice in the case when the initial

energy is transferred to a limited number of phonon branches could provide a base for a model that relates the nonequilibrium dynamics to the material properties, such as the electron-phonon coupling strength.

Few direct lattice-sensitive experiments have been performed on the cuprates, and their results are rather controversial. A previous ultrafast electron microscopy (UEM) experiment on $\text{Bi}_2\text{Sr}_2\text{CaCu}_2\text{O}_{8+\delta}$ (Bi-2212) determined (12, 13) the time scale of electrons coupling to the out-of-plane lattice vibrations to be several picoseconds, which is considerably longer than the initial steps of electronic relaxation. Another phonon-sensitive technique, wideband terahertz spectroscopy, has demonstrated (14) population growth of the out-of-plane lattice vibrations in $\text{YBa}_2\text{Cu}_3\text{O}_{7-\delta}$ (YBCO) involving the apical O ion within 150 fs—a time scale comparable to quasi-particle formation simultaneously registered in the ab plane. The a axis dynamics in $\text{La}_{2-x}\text{Sr}_x\text{CuO}_4$ (LSCO) observed with time-resolved x-ray diffraction (15) correspond to a coupling constant 40 times smaller than that extracted for Bi-2212 from tr-ARPES (4) while applying the same model. However, there has been no direct imaging of the Bi-2212 in-plane lattice response to a femtosecond laser excitation so far, although it would greatly broaden the understanding of electron-phonon interaction in the cuprates, and it would be particularly useful here because most of tr-ARPES experiments were performed on this compound.

Here, we directly connect the electron dynamics to that of the lattice in optimally doped Bi-2212 through combined megaelectron volt ultrafast electron diffraction (MeV-UED) and tr-ARPES. By comparing the time scale of the electronic energy dissipation after a femtosecond laser pulse with the time scale of the lattice response from taking up this energy, these complementary experiments are used to verify that electron-lattice coupling is indeed the channel responsible for electronic cooling. We unequivocally determine the optical phonons involved in the fast electron energy dissipation and further demonstrate that these phonons subsequently couple to other atomic vibrations, both optical and acoustic, creating a nonthermal phonon distribution that continues to evolve for more than 10 ps after the photoexcitation. In so doing, we

¹Brookhaven National Laboratory, Upton, NY 11973, USA. ²Department of Physics and Astronomy, Stony Brook University, Stony Brook, NY 11794, USA. ³Stanford Linear Accelerator Center National Accelerator Laboratory, Menlo Park, CA 94025, USA. ⁴Department of Physics, North Carolina State University, Raleigh, NC 27695, USA. ⁵Faculty of Physics and Center for Nanointegration Duisburg-Essen, University Duisburg-Essen, Duisburg 47048, Germany. ⁶Department of Physics, Georgetown University, Washington, DC 20057, USA.

*Corresponding author. Email: tatiana.konstantinova@stonybrook.edu (T.K.); zhu@bnl.gov (Y.Z.)

have defined the relaxation path from nonequilibrium to the ground state in the cuprates, an extensively studied but still not well-understood strongly correlated system.

RESULTS

Experimental approach

The initial electron diffraction work was carried out at the 2.8-MeV Brookhaven National Laboratory (BNL) UED facility (16, 17), and most of the experiments reported here were performed on the 4.0-MeV-UED setup at the Stanford Linear Accelerator Laboratory. The principle of MeV-UED operation is described elsewhere (18) and is depicted in Fig. 1A. A 100-fs laser pulse with a photon energy of 1.55 eV and a fluence of 2.0 to 10.7 mJ/cm², sufficient to produce a photoinduced change with an acceptable signal-to-noise ratio in pump-probe detection, is used to excite the sample, followed by a probe electron pulse arriving at the sample after a controlled delay. The laser and electron beams are collinear and directed along the crystal *c* axis. Experiments are done at different sample temperatures as indicated. The 100-fs resolution of our MeV-UED setup for the first time allows monitoring of the subpicosecond lattice response to electron relaxation in Bi-2212. The advantage of an electron probe is its ability to yield information about phonon modes residing within the low-energy Drude part of the electron spectrum. These modes are hard to detect with terahertz spectroscopy because of the dominance of the electronic signal in this energy

range. Mega-electron volt electron diffraction, in particular, can access high-order reflections that are more sensitive to atomic displacements than the low-order reflections usually observed with kilo-electron volt electrons. Simultaneous observation of multiple Brillouin zones and the wide dynamical range of intensities provided by the MeV-UED setup allows for the time- and momentum-resolved study of the phonon population and thus the identification of the time scales for various phonon energy scales—information that has not been obtained for the cuprates so far with other techniques.

A detailed experimental description of the tr-ARPES experiment (Fig. 1B) can be found elsewhere (19). Here, we performed 1.55-eV photoexcitation of optimally doped Bi-2212 in the normal state with incident laser fluence between 250 and 640 μJ/cm². The upper limit of the fluence is carefully chosen to avoid multiphoton photoemission and residual steady-state heating from the pump laser.

Experimental observations

The Bi-2212 crystal structure (see Materials and Methods) exhibits an incommensurate lattice modulation that gives rise to satellite peaks and peaks forbidden by the *b*-centered symmetry of the average crystal structure as seen in Fig. 1C. We will refer to all the peaks related to the incommensurate modulation as superlattice (SL) peaks. Because the Bragg and SL peaks represent different lattice orders, their response to displacements of individual atoms differs. The mechanism of the modulation formation makes SL peaks in the probed [001] plane

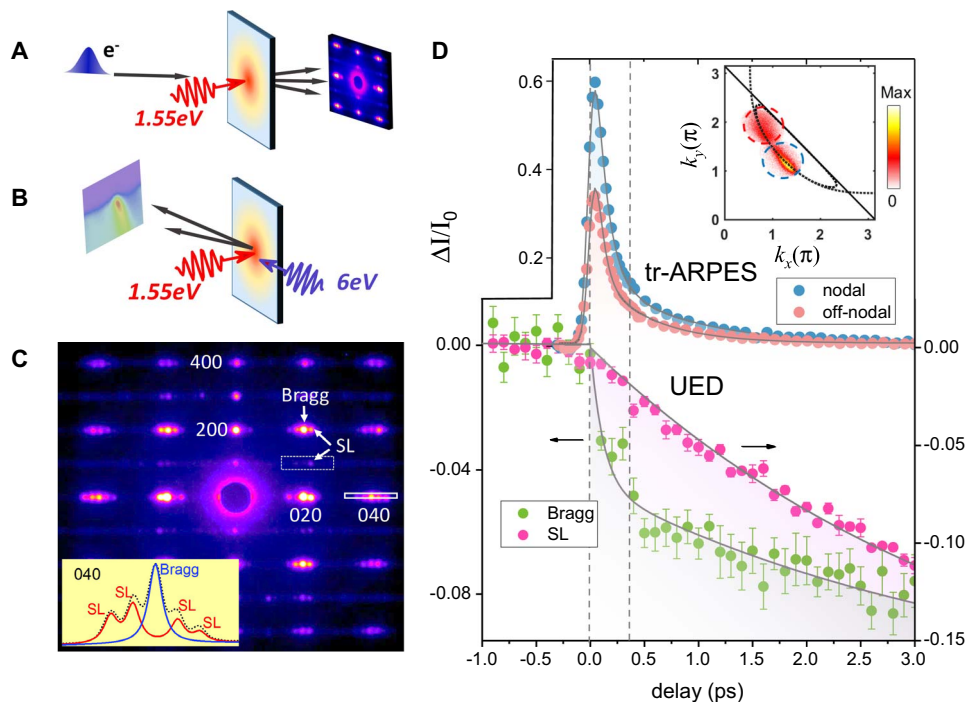


Fig. 1. Comparison of the MeV-UED and tr-ARPES techniques. Schematic of UED (A) and tr-ARPES (B) experiments. (C) Diffraction pattern of the Bi-2212 sample taken by MeV-UED. The inset shows the profile of (040) peak with central Bragg peak (blue) and satellite SL peaks (red). (D) Time-resolved dynamics of electron and phonon systems. Blue (nodal) and red (off-nodal) circles show changes of electron spectral weight obtained by tr-ARPES in different parts of the Brillouin zone. Changes of diffraction peak intensities in the MeV-UED experiment are shown by green (Bragg) and purple (SL) circles. All changes are normalized by the values before the excitation. Solid lines are fits described in Materials and Methods. Dashed lines indicate the arrival of the pump pulse (zero delay) and the turning point in electron and lattice dynamics. The inset shows equilibrium of the Fermi surface. Regions where data were taken are circled. Dotted lines show the underlying tight binding and Yang-Rice-Zhang Fermi surfaces for optimal doping. The solid line is the antiferromagnetic zone boundary. MeV-UED data are taken at 30 K, and tr-ARPES data are taken at 125 K.

specifically sensitive to atomic motion in the Bi-O layers. Figure 1D indeed shows different peak dynamics for Bragg and SL after a pump pulse at the sample temperature of 30 K in the MeV-UED measurement. The Bragg peaks experience decay with two distinct time scales: $\tau_{\text{short}}^{\text{ph}} = 0.17 \pm 0.05$ ps and $\tau_{\text{long}}^{\text{ph}} = 3.8 \pm 0.5$ ps. The fast time constant is limited by the temporal resolution of the experimental setup. The SL peak intensity drop is well described by a single time constant $\tau_{\text{long}}^{\text{ph}} = 4.0 \pm 0.2$ ps, similar to the Bragg peaks' slow (long) component, and is naturally assumed to be caused by the same process. For each peak type (Bragg and SL), the time constants of the intensity drops are the same for all in-plane ([001]) crystal directions and are smaller than that reported for the *c*-axis dynamics (13). According to previous work, the fast time scale (4, 10, 11, 20) is attributed to electrons coupling to the “hot” in-plane breathing, out-of-plane buckling, and apical oxygen vibrational modes. Because the geometry of the present experiment makes the diffraction intensity most sensitive to the atomic motion in the *ab* plane (reflections within the first-order Laue zone), we ascribe the fast time constant to an increase in the in-plane modes' population. Strong electron coupling to the in-plane Cu-O bond stretching modes in the high- T_c cuprates was inferred from neutron scattering (21), ARPES (22), x-ray absorption (23), and Raman (24) experiments. The slow time scale is attributed to the anharmonic decay of hot phonons and to the electron coupling to other lattice vibrations.

Whereas UED presents an electron momentum- and electron energy-averaged picture, tr-ARPES can provide insight into the hot electron dynamics in different regions of the Brillouin zone. The upper panel of Fig. 1D shows the dynamics of the energy-integrated hot electron population for nodal and off-nodal directions of the Brillouin zone. Both directions exhibit two-step dynamics, characterized by $\tau_{\text{short}}^{\text{el}}$ and $\tau_{\text{long}}^{\text{el}}$. The same (within experimental error) 60- to 110-fs short time constant $\tau_{\text{short}}^{\text{el}}$ is observed for both nodal and off-nodal electrons, meaning that the energy-integrated relaxation rate is largely independent of momentum direction in the measured region. This is consistent with the work of Dakovski *et al.* (25), which has shown that nodal and anti-nodal excited electron populations decay at the same rate in the normal state. Consequently, $\tau_{\text{short}}^{\text{el}}$, which corresponds (7) to coupling to bosons in a narrow energy window around 75 meV, reflects electron energy-averaged dynamics for all electron momenta, therefore allowing direct comparison with similar electron momentum- and electron energy-averaged MeV-UED results. This fast time constant $\tau_{\text{short}}^{\text{el}}$ is the same as $\tau_{\text{short}}^{\text{ph}}$ within the experimental error despite the difference in pump fluence. It is thus conceivable, in the absence of any high-excitation density phenomena, that the phonons populating at $\tau_{\text{short}}^{\text{ph}}$ observed directly in MeV-UED are the 75-meV bosonic modes identified in tr-ARPES.

One example of a high-excitation density effect was observed (13, 26) for $\text{La}_2\text{CuO}_{4+\delta}$ (another cuprate material) which undergoes a structural phase transition upon photoexcitation above the photodoping fluence threshold and experiences expansion along the *c* axis. However, such a transition, which should not (26) affect the *ab* plane, cannot play a role in the structural dynamics discussed in the present work. The photoinduced transition, observed in $\text{La}_2\text{CuO}_{4+\delta}$, involves the formation of macroscopic domains and proceeds with the characteristic time scale of 30 ps, much slower than the processes reported in this work. Moreover, the dynamics of the Bi-2212 lattice measured with the same experimental technique under the same excitation condition (13) was shown to be different from $\text{La}_2\text{CuO}_{4+\delta}$ and was dominated by the reduction of the peak intensity due to the Debye-Waller factor increase.

The slow electronic time constant $\tau_{\text{long}}^{\text{el}}$ between 0.5 and 1.0 ps, is comparable to values derived from other time-resolved optical spectro-

scopy measurements (9–11, 20) for various cuprate systems, suggesting that these experiments observe the same process. Whereas other works refer to electron and lattice temperatures, we refrain from that concept. The electronic system remains (4) far from equilibrium for several hundred femtoseconds after the pump pulse, and, as such, the electron temperature cannot be strictly defined. The same is true for the lattice. Electron-phonon coupling leads to selective population of the high-energy optical branches (4, 27, 28) not obeying a Bose-Einstein distribution and therefore compromising the conventional relation between lattice temperature and atomic displacement measured by MeV-UED.

Determination of atomic displacements with dynamical Bloch wave calculations

To verify that the Cu-O in-plane phonons are involved in subpicosecond lattice dynamics, we performed a Bloch wave simulation of the diffraction intensity changes due to various atomic displacements aimed to match the trend observed in the MeV-UED experiment. We have chosen two reference time points (Fig. 2, A and B): 0.4 and 12 ps after photoexcitation. By 0.4 ps, the fast process observed for Bragg peaks has completed, and by 12 ps, the slower process at 300 K has already brought the system to quasi-equilibrium because peak intensities reach stable values. The intensities of the peaks are calculated, on the basis of Bloch wave dynamical diffraction theory, which has proven to be extremely valuable in disentangling specific atomic motions in UED experiments (17).

In the Bloch wave approach, which takes dynamic scattering into account, the scattering strength of the crystal potential depends on the structure factor

$$\text{SF}(\mathbf{q}; \mathbf{r}_1 \dots \mathbf{r}_N) = \sum_{\mu=1}^N f_{\text{at}}^{\mu} \exp(-B^{\mu} q^2) \exp(i\mathbf{q} \cdot \mathbf{r}_{\mu}) \quad (1)$$

where f_{at}^{μ} is the atomic scattering factor (29) of atom μ ; $B^{\mu} = -(8\pi^2/3)\langle x_{\mu}^2 \rangle$ is the Debye-Waller factor, with x_{μ} being the atomic displacement; \mathbf{q} is a reciprocal lattice vector; and \mathbf{r}_{μ} is the atomic position within a unit cell. An increase in phonon population leads to growth of $\langle x_{\mu}^2 \rangle$ and, consequently, B^{μ} . By calculating the peak intensity with Eq. 1 and atomic parameters refined from neutron diffraction data (30) (but using $\mathbf{k}^* = 0.2b^* + c^*$ approximation for the modulation vector), while varying values of B^{μ} , we modeled the impact of different atomic displacements on Bragg and SL peak intensities. In particular, the effects of atomic vibrations in the Cu-O plane only and throughout the whole unit cell are compared.

The initial crystal parameters correspond to an equilibrium state at 300 K. An enhanced population of Cu-O phonons is simulated by an increase in B^{μ} factors of Cu and the in-plane neighboring O atoms by 0.2 and 0.8 \AA^2 , respectively, accounting for four times atomic mass difference, whereas the parameters of the other atoms in the unit cell are kept unchanged. This change reflects a nonthermal population of the optical phonons in the Cu-O plane. Because the slower time scale is attributed to population of all vibrational modes, the decrease of intensity at 12 ps is compared to all-atomic vibrations that are introduced as an isotropic 50% increase of B^{μ} (300 K). The change of B^{μ} factors by a fraction of the 300 K values instead of a fixed number imitates the real phonon density in the system at elevated temperature. Because local equilibrium is reached, the phonon distribution can be considered almost as thermal at this point. The results of calculations

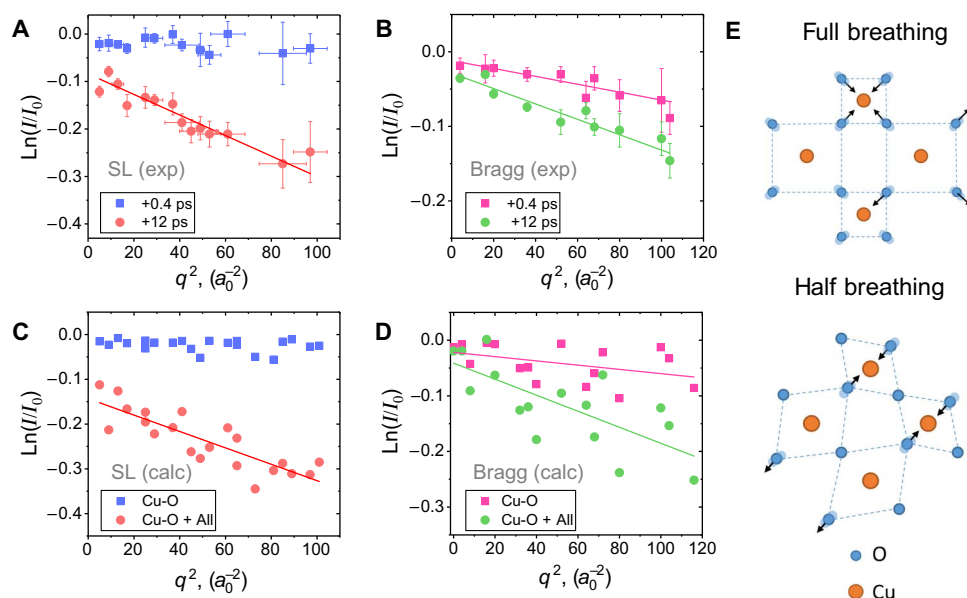


Fig. 2. Role of the Cu-O vibrations and the total phonon bath in peak intensity suppression as a function of wave vector q . Experimental SL (A) and Bragg (B) peak intensities I at 0.4 ps (blue squares for SL and pink squares for Bragg) and 12 ps (red circles for SL and green circles for Bragg) after photoexcitation, normalized by values I_0 for the unexcited sample, are plotted as functions of q^2 . Vertical bars represent statistical error, and horizontal bars result from integrating intensities over several neighboring peaks. The sample base temperature is 300 K, and the laser fluence is 10.7 mJ/cm². The intensities of SL (C) and Bragg (D) peaks for increased vibrational amplitude in the Cu-O plane (blue squares for SL and pink squares for Bragg) only and for additional increase of Debye-Waller factors of all atoms by 50% (red circles for SL and green circles for Bragg) are calculated with Bloch wave approach and normalized by I_0 at 300 K parameters. Solid lines present the linear fit for the data. (E) Schematic motion of atoms for the full-breathing and half-breathing phonon modes.

are shown in Fig. 2 (C and D). Note, that because the unit cell is not monoatomic and the Debye-Waller factors are increased by a different amount for each atom, in general, discrete values of $\ln(I/I_0)$ (q) that deviate from the overall linear trend are expected. Because of the perfect coherence of the scattering by perfectly arranged atoms considered, the simulation yields a large dispersion of the data around the linear fit. In the real situation, the coherence is limited by beam divergence and the crystal imperfections, including sample bending and mosaic domains; thus, the variations in diffraction intensities are smeared out during the multiple scattering processes, and a more linear dependence is observed.

According to the results of the calculations, the increase in Cu and O Debye-Waller factors accounts for about half of the Bragg intensity drop produced by all-atomic and Cu-O vibrations combined and leads to a negligible change in SL peaks, which have strong responses to the all-atomic displacements as expected from the modulation origin. The results resemble the trend observed in the experiment, confirming that the fast drop in the Bragg peak intensity is the outcome of increased Cu and O in-plane displacements. Slopes of the linear fit to the data shown on the graph match the experimental observations and the calculations within an error of the order 15 to 55% for the calculations and 14 to 17% for the experimental data. We conclude that the MeV-UED observations are consistent with the assumption of the fast electron energy relaxation being due to electrons coupling to the hot Cu-O phonons such as the full-breathing and half-breathing modes (shown in Fig. 2E), which were demonstrated (21, 24, 31, 32) to strongly interact with electronic excitations, and the slow process involving other atomic vibrations, primarily in the Bi-O and Sr-O planes. Thus, the difference between $\tau_{\text{short}}^{\text{ph}}$ and $\tau_{\text{long}}^{\text{ph}}$ reflects the rate of the energy transfer between the crystal layers.

Temperature and laser fluence dependence of electron and lattice dynamics

The role of electron-phonon coupling and anharmonic phonon decay in the population of the lower-energy phonon branches after the buildup of the hot phonons can be separated on the basis of the temperature and fluence dependence of the slow time constant. The phonon-phonon coupling usually proceeds faster at elevated sample temperatures, when the density of final phonon states is high (33, 34). An increase in sample temperature up to 300 K does not reveal any significant change in $\tau_{\text{short}}^{\text{ph}}$. At the same time, $\tau_{\text{long}}^{\text{ph}}$, obtained from a single-exponential fitting of the SL peak intensity, remains the same only at low temperatures but, at 300 K, has dropped to 2.5 ± 0.2 ps as shown in Fig. 3A. It was previously suggested (13) that the lattice dynamics even at high excitation densities can be affected by the superconducting electronic state. However, our data show that the slow time constant is independent of T_c . The observed behavior of $\tau_{\text{long}}^{\text{ph}}$ indicates that the slow process is likely dominated by the anharmonic phonon-phonon decay rather than electron-phonon coupling, which would show much weaker variation with sample temperature (35). A similar trend was observed for Bi-2212 c -axis dynamics at certain excitation geometries (13) and in the previous tr-ARPES experiment (4). Analogous behavior is observed for the hot optical phonon decay in graphite (36) and carbon nanotubes (37).

The study of the c -axis dynamics (12) revealed sensitivity of the temporal lattice response to the direction of pump polarization. However, we did not observe such dependence for ab plane atomic dynamics at either 30 or 300 K temperature. Changing the pump photon energy to 4.65 eV does not change the temporal lattice response either (Supplementary Materials). This agrees with the picture of energy redistribution within electronic systems during much shorter time scales than $\tau_{\text{long}}^{\text{ph}}$.

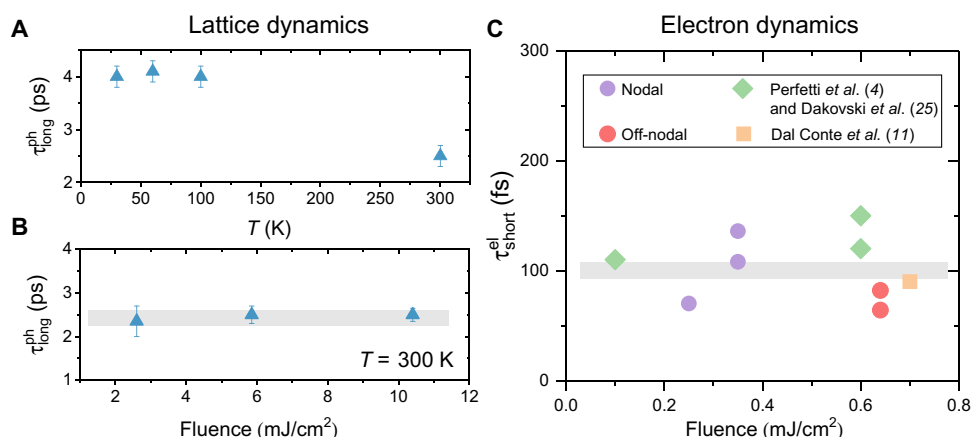


Fig. 3. Temperature and fluence dependence of electron and lattice dynamics. Values of long time constants $\tau_{\text{long}}^{\text{ph}}$ are extracted from the MeV-UED as function of sample temperature (A) and laser fluence (B). The dependence indicates that the phonon population growth after +0.5 ps is dominated by phonon-phonon anharmonic decay and not by electron-phonon coupling. (C) Values of the short time constants extracted from the tr-ARPES experimental data and given in the studies of Perfetti *et al.* (4), Dal Conte *et al.* (11), and Dakovski *et al.* (25) as a function of pump laser fluence. The difference in values for the same fluence is more likely attributed to sample variation from cleave to cleave. Gray lines in (B) and (C) are guides to the eye.

MeV-UED experiments exceed the superconducting gap evaporation threshold (38, 39), thus bringing the system to the normal metal state. Above this threshold, the dependence of the quasi-particle relaxation rate on the lattice temperatures and the laser fluence observed for low-density excitations (40–43) saturates. In the 2.7 to 10.7 mJ/cm² excitation range, $\tau_{\text{long}}^{\text{ph}}$ is observed to be constant as shown in Fig. 3B. Similarly, $\tau_{\text{long}}^{\text{ph}}$ measured with tr-ARPES, does not vary with the fluence (Supplementary Materials), which again confirms that the phonon-phonon decay, independent of the electron density of states, plays the most important role at the slow time scale.

Turning to the behavior of the fast time constant with laser fluence, we observe that $\tau_{\text{short}}^{\text{ph}}$ is resolution-limited for all measured fluences and that $\tau_{\text{short}}^{\text{el}}$ found in tr-ARPES is fluence-independent as shown in Fig. 3C. This suggests that the N -temperature model with coupling time proportional to the electron temperature is not applicable here because one would expect any effective temperature to scale with pump fluence. The same observation has also been demonstrated for other cuprates (8, 20, 41) in a wide range of excitations, which led to suggestion that a nonlinear model should be considered (20). The independence of the temporal response for the cuprates in the normal state on the pump fluence facilitates comparison of the data obtained from the tr-ARPES and MeV-UED experiments despite the unavoidable difference in excitation densities.

Determination of the phonon characteristic time scales through analysis of inelastic electron scattering

Although we have established that the slow time constants correspond to phonon-phonon coupling, the above data cannot determine how the energy redistributes among different phonon branches. Additional momentum-resolved information about the lattice dynamics can be obtained via the analysis of thermal diffuse scattering (TDS) (44), that is, the scattering of electrons by phonons, which is measured as diffuse intensities in between Bragg and SL peaks and is inversely proportional to the phonon energy.

The TDS intensity is much weaker than that of the Bragg and SL peaks, and its change due to photoexcitation can be best seen in the differential images. Figure 4 (A to C) shows the difference between the diffraction patterns obtained from the sample at certain time delays and

before arrival of the pump pulse. Each image is obtained by binning the data with 1-ps windows (10 time steps) to achieve better statistics. At +0.5-ps delay, the increase of the TDS intensity is weak as would be expected from high-energy phonon modes, involving motion of the light atoms. By +2.5 ps, the TDS intensity is much stronger and is dominated by the isotropic diffuse background. By +5.5 ps, the intensity increases still further (Fig. 4C), and, from Fig. 4D, a streak pattern starts to form on top of the diffuse background. As described in Materials and Methods, these streaks are formed by acoustic phonons with correlated atomic motion along $\langle 110 \rangle$ crystallographic directions, whereas the diffuse background is formed by optical phonons.

We identify the difference in time scale of the TDS intensity buildup due to optical and acoustic phonons, as shown in Fig. 4F. The intensity integrated over $44 \times 17 \times 17$ -pixel windows outside the streaks, influenced by optical branches, shows a time constant of 3.1 ± 0.3 ps when fitted with a single-exponential function. Note that only the optical phonons of the lowest energies, such as superstructure-associated amplitude branches (45) at 28 and 47 cm⁻¹, dominate the diffuse isotropic signal according to Eq. 4 in Materials and Methods. To obtain information about the buildup of acoustic phonons, we subtracted the above intensity from the signal, integrated over the same number of nearby windows along the streaks, which reflect scattering by both optical and acoustic phonons. A single-exponential growth fit produces the time constant of 9.5 ± 1.0 ps for the well-defined acoustic waves in the crystal. When integrated over symmetrical points of the Brillouin zone, the TDS intensity dynamics (Supplementary Materials) follow a single-exponential growth curve with a time constant coinciding with $\tau_{\text{long}}^{\text{ph}}$, meaning that $\tau_{\text{long}}^{\text{ph}}$ reflects the rise of the atomic displacements due to all low-energy phonons combined.

The TDS analysis directly shows that phonons of higher energy are populated faster than those with lower energies. This explains the two to eight times difference between $\tau_{\text{long}}^{\text{el}}$ and both $\tau_{\text{long}}^{\text{ph}}$ and the time scale of the c -axis lattice dynamics (12) that are also slower than $\tau_{\text{long}}^{\text{el}}$. In the case when the energy relaxation rate of the phonon subsystem is governed by multiple phonon-phonon interactions, the tr-ARPES is more sensitive to the upper phonon branches that are generated first by the decay of the hot phonons, which, in turn, dissipates excess electronic energy, whereas diffraction mainly picks up the slowly populating lower

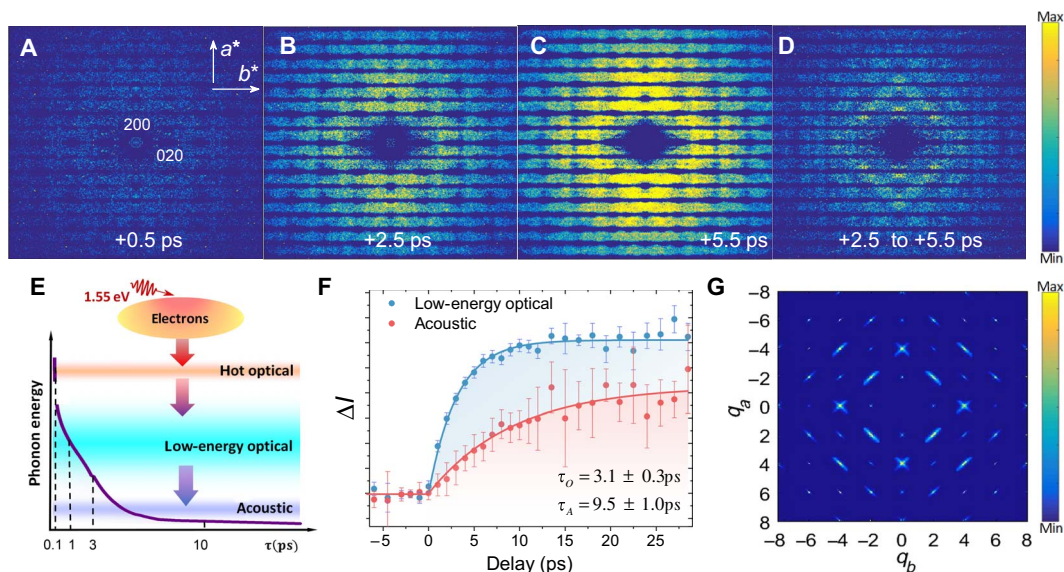


Fig. 4. Analysis of the TDS intensity dynamics. (A to C) TDS images are obtained by subtracting an average diffraction pattern of the unpumped sample from diffraction patterns at certain delays after the pump laser pulse arrival. For each image, the data are binned within a 1-ps window. Dark horizontal lines appear because of the depleted intensity of the Bragg and SL peaks. (D) Difference between (C) and (B). A streak pattern begins to form on top of the diffuse background. Images (A) to (D) share the same range of intensities, color-coded according to the scale on the left. (E) Scheme of energy transfer between electronic and phonon systems upon photoexcitation. The purple curve represents the schematic evolution of the characteristic time scales of the phonon buildup as a function of the phonon energy. (F) Intensity dynamics of TDS of the low-energy optical (blue) and acoustic (red) phonons. The solid lines are single-exponential growth fits. (G) Intensity distribution of TDS due to the acoustic phonons calculated with Eqs. 4 and 5.

branches that produce larger displacements or involve heavy atoms with high scattering power.

The growth rate of phonon population

The observed $\tau_{\text{short}}^{\text{ph}}$ is one order of magnitude smaller than the time measured for incoherent phonon population growth in normal metals (46–48). However, it is comparable to the time scale of the increase in strongly coupled optical phonon modes in graphene (27) and graphite (49). To verify whether the hot phonon population can grow on the 100-fs scale, we consider a theoretical simulation of an interacting electron-phonon system using a nonequilibrium Keldysh approach (50). The calculations consist of a tight-binding system of electrons coupled to a bath of Einstein phonons. The system is excited by a short pump pulse that directly deposits energy into the electrons by driving a current. The energy is subsequently transferred to the phonons until a balance is achieved between the electrons and the phonon bath (51). This naturally leads to a nontrivial time dependence of the deposited electron energy, that is, an exponential decay with a constant rate does not capture the physics.

Figure 5A shows the average phonon displacement $\langle X^2 \rangle$, the change in the electron population ΔN , and energy ΔE_{el} above E_F as a function of time. The probe resolution of the simulation is chosen to be the same as in the experiments to provide an illustrative comparison. Previously, it was argued that the rate of energy transfer is the determining factor in the electron system's return to equilibrium (7). To show that this remains the case when the phonon degrees of freedom are affected (the $\langle X^2 \rangle$ increased), we assume that the data can be modeled (at each point in time) with a decaying exponential and extract the decay rates τ^{-1} , which are plotted in Fig. 5B. The growth rate of the phonons eventually matches the decay rate of the excess energy in the electronic system, indicating that the phonon population dynamics are also determined by the rate of energy transfer between the electrons and phonons. Con-

sequently, the growth of the phonon population occurs on the same time scale as the electron energy equilibration. This provides theoretical confirmation for the intuitive relationship between the lattice and electron time scales observed experimentally.

DISCUSSION

The present study allows us to reconstruct the picture of the redistribution of excess energy, deposited by the laser, from electrons to the lattice and within the phonon system in strongly correlated Bi-2212. The energy flow is illustrated in Fig. 4G. The similarity of the fast time scales of the electron spectral weight relaxation and the atomic displacements leads to the conclusion that, within the first 400 fs, the MeV-UED and tr-ARPES experiments observe the same process, namely, the exchange of energy between electrons and lattice. The large heat capacity of the lattice allows for considerable heat absorption within a few hundred femtoseconds even at the very high excitation fluences applied in the experiments. An analysis of the MeV-UED data based on the Bloch wave calculations demonstrates that the extremely fast response of the Bragg peaks to photoexcitation is due to the strong electron coupling to the Cu-O in-plane displacements. Because it was shown before (7) that a limited subset of bosons in a narrow energy range around 75 meV dominates the electron dynamics at 100-fs time scale, it is reasonable to ascribe the observed motion of Cu and O to the Cu-O in-plane bond stretching phonons that have the same energy (52). Our calculations show that a single phonon mode is populated at a 100-fs scale while removing energy from the electron subsystem. This selective coupling creates a highly nonthermal distribution of phonons, with most of the deposited energy concentrated into one or several hot phonon branches. Through temperature and fluence dependence of the lattice response, we have shown that coupling of electrons to other branches is weak and is overrun by an anharmonic decay of the hot

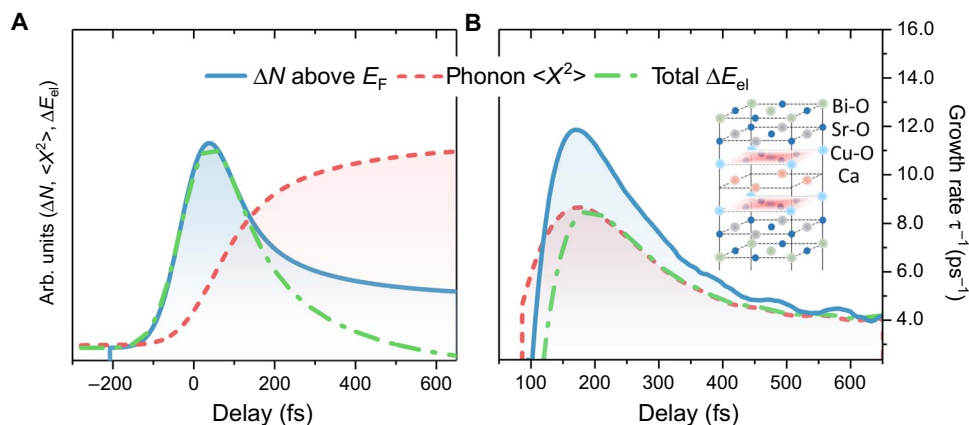


Fig. 5. Theoretical prediction of electron and lattice dynamics. (A) Time evolution of excited electron population ΔN , averaged phonon displacement squared $\langle X^2 \rangle$, and electron excess energy ΔE_{el} above E_F obtained by the simulations shows that the electron and the lattice dynamics happen on the same time scale. (B) Dynamics rates, extracted from exponential fit of the data in (A) at every time point, as functions of time for the parameters presented in (A). The simulations show that the rate of the phonon population growth is governed by the rate of the energy exchange between the electron and the phonon. The energy exchange at the subpicosecond time scale is limited to the Cu-O plane, highlighted in the inset.

phonons. The subpicosecond time scale of the electron coupling to the hot phonons is independent of excitation fluence, which was confirmed by directly monitoring the evolution of electronic subsystem in the present work and previous experiments (8, 20, 41, 53) for other cuprates. The observation contradicts the N -temperature model and confirms that electron-lattice energy exchange upon photoexcitation in high- T_c cuprates, even for the normal state, is different from that in conventional metals where the two-temperature model is applicable, whereas more advanced models (54, 55) have also been suggested. Lack of dependence on the pump fluence for the short time scale likely arises from the fact that the hot phonons populate, while the electronic system remains in a nonequilibrium state, similar to that observed (14) for superconducting YBCO.

The energy initially accumulated in a few (or even a single) high-energy optical branches later redistributes through anharmonic phonon-phonon coupling at different rates among the optical branches of lower energies and acoustic phonons, which subsequently further decay before reaching the final thermal equilibrium. During this process, the energy flows from the Cu-O plane toward other atomic layers due to population of out-of-plane vibrations, which proceeds (13) on a time scale comparable to the difference between τ_{long}^{ph} and τ_{short}^{ph} , and transverse branches propagating along the c axis. Slow population of lower-energy phonons creates the bottleneck regime, where electrons and hot phonons store equal amounts of energy. The last step of the lattice thermalization process, proceeding with the characteristic time scale of 10 ps, is the formation of the acoustic waves with atomic motion along the $\langle 110 \rangle$ crystal directions. It is these waves that give rise to the streak pattern in the diffraction. We explain the mismatch between τ_{long}^{el} and τ_{long}^{ph} by the sensitivity of the techniques to the different stages of the energy redistribution process. The difference in the characteristic slow time scales for LSCO measured by time-resolved x-ray diffraction (15) and optical reflectivity (20) also fits this picture because x-ray diffraction, similar to electron diffraction, is more sensitive to low-energy phonons, which produce larger atomic displacements than higher-energy branches. The fluence independence of the time response along with the sensitivity to the phonons of different energies helps to explain the huge mismatch of the electron-phonon coupling constants in cuprates previously extracted from time-resolved x-ray diffraction (15) and

tr-ARPES (4) through the use of the three-temperature model. Our MeV-UED results show that the higher-energy phonon branches populate faster than the lower-energy ones, an indication that phonons do not obey the Bose-Einstein distribution for 10 ps after the photoexcitation. Thus, at this time scale, the concept of lattice temperature is not well defined even if the hot phonons are considered as a separate thermal bath.

In conclusion, the combination of MeV-UED and tr-APRES techniques has been applied to study the nonequilibrium dynamics in the strongly correlated Bi-2212. The comparison of electronic and lattice responses and analysis based on the Bloch wave calculations and momentum-resolved examination of the TDS intensity allows for the determination of the energy flow path from the photon absorption by electrons to the formation of the acoustic phonons, while the system comes to a quasi-equilibrium. The Cu-O bond stretching in-plane phonons are identified as high-energy optical branches involved in the electron relaxation on the 100- to 400-fs time scale. The fast buildup of the optical branches and the slow buildup of acoustic branches indicate a nonthermal phonon distribution along the path, which, together with other arguments, questions the validity of the N -temperature model for a quantitative analysis of the nonequilibrium dynamics in the cuprates. The integrated approach separates the role of the lattice from other many-body excitations in the electron relaxation and can be beneficial for studying other strongly correlated systems where such separation is essential. Although the present study provides the experimental data revealing the nonequilibrium redistribution of excess energy in strongly correlated systems such as the cuprates and yields a qualitative picture of the electron-lattice interactions, it does not establish the quantitative connection between observed unconventional system dynamics and static material properties, for example, electron-phonon coupling and superconductivity. Further theoretical development in that field is necessary.

MATERIALS AND METHODS

Sample preparation

The tr-APRES and UED experiments were performed on single crystals of optimally doped Bi-2212 ($T_c = 91$ K). Results presented are from

samples obtained from a single batch grown by the floating zone method. T_c was confirmed in all cases by superconducting quantum interference device magnetometry. Samples used for tr-ARPES (about 1 mm², 0.5 mm thick) were cleaved in situ by the top post method near the lower lattice equilibrium temperature of ~110 K, in a base vacuum of 5×10^{-11} mbar. Although tr-ARPES measurements from two samples are presented here, they are typical of results from a number of measurements.

For MeV-UED experiments, flakes with an average thickness around 100 nm (determined with electron energy loss spectroscopy) were exfoliated from a single crystal using Scotch tape and placed on molybdenum grids after dissolving the tape in acetone. Penetration length of the 1.55 eV measured with ellipsometry was 109 to 116 nm depending on the light polarization. The laser beam was focused down to 300- μ m root mean square (RMS) on the sample, and the electron beam size was 70- μ m RMS. Consequently, the samples were uniformly excited in the probed volume.

Crystal structure

Bi-2212 has a centrosymmetric $NBmb/\bar{1}\bar{1}1$ symmetry with the following unit cell parameters (30): $a = 5.401$ Å, $b = 5.397$ Å, and $c = 30.78$ Å. The lattice exhibits an incommensurate modulation (56) with the wave vector $\mathbf{k}^* = 0.21\mathbf{b}^* + \mathbf{c}^*$, where \mathbf{b}^* and \mathbf{c}^* are reciprocal lattice unit vectors. The reason for the modulation is reported to be the mismatch between Bi–O and Cu–O bond length (57), which leads to displacements of all the atoms from their average positions, with atoms in the Bi–O plane being shifted mainly along the b direction and atoms in the Cu–O plane moved along the c axis. Thus, a small dependence of the ab plane SL peaks on the Cu and O displacements is anticipated. Atoms in the Bi–O plane have the largest influence on the SL peak intensities.

Data analysis

For MeV-UED experiments, the time constants for the Bragg peaks were extracted from a biexponential decay fit

$$\Delta I/I_0 = A_{\text{ph}} \left(\exp\left(\frac{-t}{\tau_{\text{short}}^{\text{ph}}}\right) - 1 \right) + B_{\text{ph}} \left(\exp\left(\frac{-t}{\tau_{\text{long}}^{\text{ph}}}\right) - 1 \right) \quad (2)$$

The time constant for the SL peaks was extracted with a single-exponential decay.

For tr-ARPES, the data were fitted with the equation

$$I(t) = G(t, \sigma) \otimes \theta(-t) \left(A_{\text{el}} \exp\left(\frac{-t}{\tau_{\text{short}}^{\text{el}}}\right) + B_{\text{el}} \exp\left(\frac{-t}{\tau_{\text{long}}^{\text{el}}}\right) \right) + I_0 \quad (3)$$

where $I(t)$ and I_0 are photoelectron intensities at time delay t and before arrival of the pump pulse, respectively, $G(t, \sigma)$ is the Gaussian profile of experimental pump-probe cross-correlation with full width at half maximum $\sigma = 100$ fs, and $\theta(-t)$ is the Heaviside function. σ was determined from the photoelectron intensity dynamics at energies around 1.5 eV.

tr-ARPES measurements

As described in earlier work (7, 19), pump pulses of 800-nm wavelength and 40-fs duration, at 250-kHz repetition rate, were produced by a Coherent RegA 9040 regenerative Ti:Sapphire amplifier. The 200-nm

probe beam was produced as the fourth harmonic of part of the RegA's 800-nm fundamental using nonlinear crystals (4). The pump-probe cross-correlation was determined to be 100 fs at the sample surface. Photoelectron spectra with an overall energy resolution of 55 meV, set by the bandwidth of the laser pulses, were recorded using both angle-integrating time-of-flight (TOF) and position-sensitive TOF (pTOF) (58) electron spectrometers. The momentum resolution of the pTOF was 0.0025 Å⁻¹, and the angular acceptance of the TOF was $\pm 3^\circ$.

TDS analysis

For megaelectron volt electrons in thin samples, where the probability of multiple inelastic scattering of electrons is relatively low (Supplementary Materials), the TDS intensity can be directly related to the phonon populations at the same scattering vector (even for the case of multiple elastic scattering) and the pattern of TDS can be predicted from kinematical approximation. According to the first-order kinematical approximation (59), at every point $\mathbf{q} = (q_a, q_b)$ of the reciprocal space, the intensity of the TDS pattern, which is the incoherent sum over all atomic oscillations, depends on the phonon frequency ω_j and the population n_j of each j^{th} phonon mode

$$I_{\text{TDS}}(\mathbf{q}) \sim \sum_j \frac{1}{\omega_j(\mathbf{q})} \left(n_j(\mathbf{q}) + \frac{1}{2} \right) |F_j(\mathbf{q})|^2 \quad (4)$$

where $F_j(\mathbf{q})$ is the one-phonon structure factor

$$F_j(\mathbf{q}) = \sum_{\mu=1}^N \frac{f_{\text{at}}^{\mu}}{\sqrt{m_{\mu}}} \exp(-B_{j,\mu} q^2) (\mathbf{q} \cdot \mathbf{e}_{\mathbf{q}-\mathbf{K}_q,j,\mu}) e^{-i\mathbf{K}_q \cdot \mathbf{r}_{\mu}} \quad (5)$$

The sum is over all atoms μ . f_{at}^{μ} are the atomic scattering factors (29); m_{μ} are atomic masses; $B_{j,\mu}$ are the phonon-specific Debye-Waller factors that are inversely proportional to m_{μ} ; $\mathbf{e}_{\mathbf{q}-\mathbf{K}_q,j,\mu}$ is the polarization vector, associated with the μ^{th} atom; \mathbf{K}_q is the nearest reciprocal lattice vector to \mathbf{q} ; and \mathbf{r}_{μ} is the atomic position within the unit cell. From Eq. 5, the scattering is dominated by Bi, the heaviest element in the unit cell, because of the large atomic scattering factor and small Debye-Waller factor.

From Eq. 4, the phonons may leave specific imprints in the diffraction pattern. In the case of optical phonons, whose energy almost does not change with q approaching zero, only a diffuse background is expected, agreeing with what was observed at +2.5-ps delay. Acoustic branches, on the other hand, can form sharp streaks because their frequencies tend to zero at small q . In the case of acoustic phonons, the polarization $\mathbf{e}_{\mathbf{q}-\mathbf{K}_q,j,\mu} = \mathbf{e}_j$ is independent of the atom. Using analogy with the monoatomic case and the unit cell parameters $b \approx a$, the phonon dispersion within a single Brillouin zone can be approximated as $\omega_{\pm}^2(\mathbf{q}) = \alpha \sin^2(\pi a/2(q_a \pm q_b)) + \beta \sin^2(\pi a/2(q_a \mp q_b))$, where α and β are material-specific parameters, related to the force constants between atoms and atomic masses. The polarization vectors are $\mathbf{e}_{\pm} = 1/\sqrt{2}(1, \pm 1)$. Calculation of the intensity, generated by the phonons with these frequencies, using Eqs. 4 and 5 and the crystal parameters from the neutron diffraction data (30) demonstrates (Fig. 4E) that the streaks are expected along the $\langle 110 \rangle$ directions—the same as observed in the experiment. The phonon population is considered as constant because it does not determine the direction of the streaks. Multiple scattering, effect of beam convergence, and convolution with the SL peaks—omitted in the above calculations—affect the intensity and the width of the streaks but

not their directions (44). Consequently, the acoustic phonons with correlated atomic motion along $\langle 110 \rangle$ crystal directions explain the formation of the streaks in Fig. 4D. Note that, although the Bi atoms dominate the signal, their motion is nevertheless indicative of the total occupation of the acoustic phonons because those involve the whole crystal.

Growth rate simulation

We simulated the time evolution of the coupled electron-phonon system subjected to a temporal laser pump field. The electrons reside in the two-dimensional tight-binding band with the (next) nearest-neighbor hopping strengths (t_0) t and the chemical potential μ . The energy of the band is given by

$$\varepsilon(k) = -2t(\cos(k_x) + \cos(k_y)) + 4t_0\cos(k_x)\cos(k_y) - \mu \quad (6)$$

Here, we chose the parameters to be $t = 0.25$ eV, $t_0 = 0.075$ eV, and $\mu = 0.255$ eV (appropriate for a simplified model of hole-doped cuprates). The initial temperature of the electrons interacting with dispersionless phonons of frequency $\Omega_0 = 0.1$ eV via a coupling $\sqrt{0.02}$ eV is set to $T = 0.01$ eV (120 K).

The pump laser field was incorporated according to Peierls' substitution as $k \rightarrow k - \frac{e}{c}A(t)$, where the spatially uniform vector potential is directed along the diagonal in momentum space

$$A(t) = \frac{F_{\max}}{\omega_p} \sin(\omega_p t) \exp\left(-\frac{(t-t_0)^2}{2\sigma_p^2}\right) \quad (7)$$

where e and c are the electron charge and the speed of light. The pump field with $\sigma_p = 10$ fs width and centered at $t_0 = 0$ has the strength $F_{\max} = 0.75$ eV and frequency $\omega_p = 0.5$ eV.

The simulations are based on the evaluation of the Dyson equation for the electron and phonon propagators $G_c^k(t, t')$ and $D_c^k(t, t')$, respectively. The interactions were treated through the self-consistent Born approximation for both electrons and phonons. The electron energy was obtained from the lesser propagators as

$$E_{\text{el}} = -i \sum_k \lim_{t' \rightarrow t} \frac{\partial}{\partial t} G_c^k(t, t') \quad (8)$$

and the phonon energy was derived in a similar way.

The population of electrons above E_F was also obtained from the lesser Green's function

$$\Delta N(t) = -i \sum_{k > k_F} G_c^k(-t, -t) \quad (9)$$

$\langle X^2 \rangle$ is found via similar derivatives of the phonon propagator (60)

SUPPLEMENTARY MATERIALS

Supplementary material for this article is available at <http://advances.sciencemag.org/cgi/content/full/4/4/eaap7427/DC1>

note S1. Bragg and SL intensity dynamics up to 55-ps delay

note S2. Fluence dependence of $\tau_{\text{long}}^{\text{el}}$

note S3. MeV-UED measurements with 4.65-eV pump

note S4. Validity of single inelastic scattering for the TDS analysis

note S5. TDS dynamics along symmetrical points of a Brillouin zone

fig. S1. Lattice dynamics at large delays.

fig. S2. Values of long time constants $\tau_{\text{long}}^{\text{el}}$ extracted from the tr-ARPES as function of laser fluence.

fig. S3. Lattice dynamics after 4.65-eV photon excitation.

fig. S4. Evolution of the TDS at Y points of the tetragonal Brillouin zone for 30 K (red circles) and 300 K (blue circles) and the exponential growth fits of the data (solid lines).

REFERENCES AND NOTES

1. C. Giannetti, M. Capone, D. Fausti, M. Fabrizio, F. Parmigiani, D. Mihailovic, Ultrafast optical spectroscopy of strongly correlated materials and high-temperature superconductors: A non-equilibrium approach. *Adv. Phys.* **65**, 58–238 (2016).
2. D. M. Newns, C. C. Tsuei, Fluctuating Cu–O–Cu bond model of high-temperature superconductivity. *Nat. Phys.* **3**, 184–191 (2007).
3. I. Madan, T. Kurosawa, Y. Toda, M. Oda, T. Mertelj, D. Mihailovic, Evidence for carrier localization in the pseudogap state of cuprate superconductors from coherent quench experiments. *Nat. Commun.* **6**, 6958 (2015).
4. L. Perfetti, P. A. Loukakos, M. Lisowski, U. Bovensiepen, H. Eisaki, M. Wolf, Ultrafast electron relaxation in superconducting $\text{Bi}_2\text{Sr}_2\text{CaCu}_2\text{O}_{8+\delta}$ by time-resolved photoelectron spectroscopy. *Phys. Rev. Lett.* **99**, 197001 (2007).
5. D. Fausti, R. I. Tobey, N. Dean, S. Kaiser, A. Dienst, M. C. Hoffmann, S. Pyon, T. Takayama, H. Takagi, A. Cavalleri, Light-induced superconductivity in a stripe-ordered cuprate. *Science* **331**, 189–191 (2011).
6. R. Cortés, L. Rettig, Y. Yoshida, H. Eisaki, M. Wolf, U. Bovensiepen, Momentum-resolved ultrafast electron dynamics in superconducting $\text{Bi}_2\text{Sr}_2\text{CaCu}_2\text{O}_{8+\delta}$. *Phys. Rev. Lett.* **107**, 097002 (2011).
7. J. D. Rameau, S. Freutel, A. F. Kemper, M. A. Sentef, J. K. Freericks, I. Avigo, M. Ligges, L. Rettig, Y. Yoshida, H. Eisaki, J. Schneeloch, R. D. Zhong, Z. J. Xu, G. D. Gu, P. D. Johnson, U. Bovensiepen, Energy dissipation from a correlated system driven out of equilibrium. *Nat. Commun.* **7**, 13761 (2016).
8. C. L. Smallwood, W. Zhang, T. L. Miller, G. Affeldt, K. Kurashima, C. Jozwiak, T. Noji, Y. Koike, H. Eisaki, D.-H. Lee, R. A. Kaindl, A. Lanzara, Influence of optically quenched superconductivity on quasiparticle relaxation rates in $\text{Bi}_2\text{Sr}_2\text{CaCu}_2\text{O}_{8+\delta}$. *Phys. Rev. B* **92**, 161102(R) (2015).
9. S. D. Brorson, A. Kazeroonian, D. W. Face, T. K. Cheng, G. L. Doll, M. S. Dresselhaus, G. Dresselhaus, G. Dresselhaus, E. P. Ippen, T. Venkatesan, X. D. Wu, A. Inam, Femtosecond thermomodulation study of high- T_c superconductors. *Solid State Commun.* **74**, 1305–1308 (1990).
10. S. Dal Conte, C. Giannetti, G. Coslovich, F. Cilento, D. Bossini, T. Abebaw, F. Banfi, G. Ferrini, H. Eisaki, M. Greven, A. Damascelli, D. van der Marel, F. Parmigiani, Disentangling the electronic and phononic glue in a high- T_c superconductor. *Science* **335**, 1600–1603 (2012).
11. S. Dal Conte, L. Vidmar, D. Golež, M. Mierzejewski, G. Soavi, S. Peli, F. Banfi, G. Ferrini, R. Comin, B. M. Ludbrook, L. Chauviere, N. D. Zhigadlo, H. Eisaki, M. Greven, S. Lupi, A. Damascelli, D. Brida, M. Capone, J. Bonča, G. Cerullo, C. Giannetti, Snapshots of the retarded interaction of charge carriers with ultrafast fluctuations in cuprates. *Nat. Phys.* **11**, 421–426 (2015).
12. F. Carbone, D.-S. Yang, E. Giannini, A. H. Zewail, Direct role of structural dynamics in electron-lattice coupling of superconducting cuprates. *Proc. Natl. Acad. Sci. U.S.A.* **105**, 20161–20166 (2008).
13. F. Carbone, N. Gedik, J. Lorenzana, A. H. Zewail, Real-time observation of cuprates structural dynamics by ultrafast electron crystallography. *Adv. Condens. Matter Phys.* **2010**, 958618 (2010).
14. A. Pashkin, M. Porer, M. Beyer, K. W. Kim, A. Dubroka, C. Bernhard, X. Yao, Y. Dagan, R. Hackl, A. Erb, J. Demsar, R. Huber, A. Leitenstorfer, Femtosecond response of quasiparticles and phonons in superconducting $\text{YBa}_2\text{Cu}_3\text{O}_{7-\delta}$ studied by wideband terahertz spectroscopy. *Phys. Rev. Lett.* **105**, 067001 (2010).
15. B. Mansart, M. J. G. Cottet, G. F. Mancini, T. Jarlborg, S. B. Dugdale, S. L. Johnson, S. O. Mariager, C. J. Milne, P. Beaud, S. Grübel, J. A. Johnson, T. Kubacka, G. Ingold, K. Prsa, H. M. Ronnow, K. Conder, E. Pomjakushina, M. Chergui, F. Carbone, Temperature-dependent electron-phonon coupling in $\text{La}_{2-x}\text{Sr}_x\text{CuO}_4$ probed by femtosecond x-ray diffraction. *Phys. Rev. B* **88**, 054507 (2013).
16. P. Zhu, Y. Zhu, Y. Hidaka, L. Wu, J. Cao, H. Berger, J. Geck, R. Kraus, S. Pjerov, Y. Shen, R. I. Tobey, J. P. Hill, X. J. Wang, Femtosecond time-resolved MeV electron diffraction. *New J. Phys.* **17**, 063004 (2015).
17. J. Li, W.-G. Yin, L. Wu, P. Zhu, T. Konstantinova, J. Tao, J. Yang, S.-W. Cheong, F. Carbone, J. A. Misewich, J. P. Hill, X. Wang, R. J. Cava, Y. Zhu, Dichotomy in ultrafast atomic dynamics as direct evidence of polaron formation in manganites. *NPJ Quant. Mater.* **1**, 16026 (2016).
18. S. P. Weathersby, G. Brown, M. Centurion, T. F. Chase, R. Coffee, J. Corbett, J. P. Eichner, J. C. Frisch, A. R. Fry, M. Gühr, N. Hartmann, C. Hast, R. Hettel, R. K. Jobe, E. N. Jongeward,

- J. R. Lewandowski, R. K. Li, A. M. Lindenberg, I. Makasyuk, J. E. May, D. McCormick, M. N. Nguyen, A. H. Reid, X. Shen, K. Sokolowski-Tinten, T. Vecchione, S. L. Vetter, J. Wu, J. Yang, H. A. Dürr, X. J. Wang, Mega-electron-volt ultrafast electron diffraction at SLAC National Accelerator Laboratory. *Rev. Sci. Instrum.* **86**, 073702 (2015).
19. J. D. Rameau, S. Freutel, L. Rettig, I. Avigo, M. Ligges, Y. Yoshida, H. Eisaki, J. Schneeloch, R. D. Zhong, Z. J. Xu, G. D. Gu, P. D. Johnson, U. Bovensiepen, Photoinduced changes in the cuprate electronic structure revealed by femtosecond time- and angle-resolved photoemission. *Phys. Rev. B* **89**, 115115 (2014).
20. C. Gadermaier, A. S. Alexandrov, V. V. Kabanov, P. Kusar, T. Mertelj, X. Yao, C. Manzoni, D. Brida, G. Cerullo, D. Mihailovic, Electron-phonon coupling in high-temperature cuprate superconductors determined from electron relaxation rates. *Phys. Rev. Lett.* **105**, 257001 (2010).
21. R. J. McQueeney, Y. Petrov, T. Egami, M. Yethiraj, G. Shirane, Y. Endoh, Anomalous dispersion of LO phonons in $\text{La}_{1.85}\text{Sr}_{0.15}\text{CuO}_4$ at low temperatures. *Phys. Rev. Lett.* **82**, 628–631 (1999).
22. Z.-X. Shen, A. Lanzara, S. Ishihara, N. Nagaosa, Role of the electron-phonon interaction in the strongly correlated cuprate superconductors. *Philos. Mag. B* **82**, 1349–1368 (2002).
23. N. L. Saini, H. Oyanagi, A. Lanzara, D. Di Castro, S. Agrestini, A. Bianconi, F. Nakamura, T. Fujita, Evidence for local lattice fluctuations as a response function of the charge stripe order in the $\text{La}_{1.48}\text{Nd}_{0.4}\text{Sr}_{0.12}\text{CuO}_4$ system. *Phys. Rev. B* **64**, 132510 (2001).
24. S. Sugai, H. Suzuki, Y. Takayanagi, T. Hosokawa, N. Hayamizu, Carrier-density-dependent momentum shift of the coherent peak and the LO phonon mode in p -type high- T_c superconductors. *Phys. Rev. B* **68**, 184504 (2003).
25. G. L. Dakovski, T. Durakiewicz, J.-X. Zhu, P. S. Riseborough, G. Gu, S. M. Gilbertson, A. Taylor, G. Rodriguez, Quasiparticle dynamics across the full Brillouin zone of $\text{Bi}_2\text{Sr}_2\text{CaCu}_2\text{O}_{8+\delta}$ traced with ultrafast time and angle-resolved photoemission spectroscopy. *Struct. Dyn.* **2**, 054501 (2015).
26. N. Gedik, D.-S. Yang, G. Logvenov, I. Bozovic, A. H. Zewail, Nonequilibrium phase transitions in cuprates observed by ultrafast electron crystallography. *Science* **316**, 425–429 (2007).
27. R. P. Chatelain, V. R. Morrison, B. L. M. Klarenaar, B. J. Siwick, Coherent and incoherent electron-phonon coupling in graphite observed with radio-frequency compressed ultrafast electron diffraction. *Phys. Rev. Lett.* **113**, 235502 (2014).
28. M. Eichberger, H. Schäfer, M. Krumova, M. Beyer, J. Demsar, H. Berger, G. Moriena, G. Sciaini, R. J. D. Miller, Snapshots of cooperative atomic motions in the optical suppression of charge density waves. *Nature* **468**, 799–802 (2010).
29. A. J. C. Wilson, E. Prince, *International Tables for Crystallography, Volume C: Mathematical, Physical and Chemical Tables* (Springer Netherlands, ed. 2, 1999).
30. P. A. Miles, S. J. Kennedy, G. J. McIntyre, G. D. Gu, G. J. Russell, N. Koshizuka, Refinement of the incommensurate structure of high quality Bi-2212 single crystals from a neutron diffraction study. *Physica C Supercond.* **294**, 275–288 (1998).
31. B. I. Kochelaev, J. Sichelschmidt, B. Elschner, W. Lemor, A. Loidl, Intrinsic EPR in $\text{La}_{2-x}\text{Sr}_x\text{CuO}_4$: Manifestation of three-spin polarons. *Phys. Rev. Lett.* **79**, 4274–4277 (1997).
32. D. Reznik, L. Pintschovius, M. Ito, S. Iikubo, M. Sato, H. Goka, M. Fujita, K. Yamada, G. D. Gu, J. M. Tranquada, Electron-phonon coupling reflecting dynamic charge inhomogeneity in copper oxide superconductors. *Nature* **440**, 1170–1173 (2006).
33. P. G. Klemens, Anharmonic decay of optical phonons. *Phys. Rev.* **148**, 845 (1966).
34. B. K. Ridley, The LO phonon lifetime in GaN. *J. Phys. Condens. Matter* **8**, L511 (1996).
35. P. B. Allen, Theory of thermal relaxation of electrons in metals. *Phys. Rev. Lett.* **59**, 1460–1463 (1987).
36. M. Scheuch, T. Kampfrath, M. Wolf, K. von Volkman, C. Frischkorn, L. Perfetti, Temperature dependence of ultrafast phonon dynamics in graphite. *Appl. Phys. Lett.* **99**, 211908 (2011).
37. I. Chatzakis, H. Yan, D. Song, S. Berciaud, T. F. Heinz, Temperature dependence of the anharmonic decay of optical phonons in carbon nanotubes and graphite. *Phys. Rev. B* **83**, 205411 (2011).
38. C. Giannetti, G. Coslovich, F. Cilento, G. Ferrini, H. Eisaki, N. Kaneko, M. Greven, F. Parmigiani, Discontinuity of the ultrafast electronic response of underdoped superconducting $\text{Bi}_2\text{Sr}_2\text{CaCu}_2\text{O}_{8+\delta}$ strongly excited by ultrashort light pulses. *Phys. Rev. B* **79**, 224502 (2009).
39. W. Zhang, C. Hwang, C. L. Smallwood, T. L. Miller, G. Affeldt, K. Kurashima, C. Jozwiak, H. Eisaki, T. Adachi, Y. Koike, D.-H. Lee, A. Lanzara, Ultrafast quenching of electron-boson interaction and superconducting gap in a cuprate superconductor. *Nat. Commun.* **5**, 4959 (2014).
40. N. Gedik, P. Blake, R. C. Spitzer, J. Orenstein, R. Liang, D. A. Bonn, W. N. Hardy, Single-quasiparticle stability and quasiparticle-pair decay in $\text{YBa}_2\text{Cu}_3\text{O}_{6.5}$. *Phys. Rev. B* **70**, 014504 (2003).
41. P. Kusar, V. V. Kabanov, J. Demsar, T. Mertelj, S. Sugai, D. Mihailovic, Controlled vaporization of the superconducting condensate in cuprate superconductors by femtosecond photoexcitation. *Phys. Rev. Lett.* **101**, 227001 (2008).
42. G. P. Segre, N. Gedik, J. Orenstein, D. A. Bonn, R. Liang, W. N. Hardy, Photoinduced changes of reflectivity in single crystals of $\text{YBa}_2\text{Cu}_3\text{O}_{6.5}$ (Ortho II). *Phys. Rev. Lett.* **88**, 137001 (2002).
43. G. Coslovich, C. Giannetti, F. Cilento, S. Dal Conte, G. Ferrini, P. Galinetto, M. Greven, H. Eisaki, M. Raichle, R. Liang, A. Damascelli, F. Parmigiani, Evidence for a photoinduced nonthermal superconducting-to-normal-state phase transition in overdoped $\text{Bi}_2\text{Sr}_2\text{Ca}_{0.92}\text{Y}_{0.08}\text{Cu}_2\text{O}_{8+\delta}$. *Phys. Rev. B* **83**, 064519 (2011).
44. Z. L. Wang, *Elastic and Inelastic Scattering in Electron Diffraction and Imaging* (Plenum Press, 1995), pp. 448.
45. R. Liu, M. V. Klein, P. D. Han, D. A. Payne, Raman-scattering from A_g and B_{1g} phonons in $\text{Bi}_2\text{Sr}_2\text{Ca}_{n-1}\text{Cu}_n\text{O}_{2n+4}$ ($n = 1, 2$). *Phys. Rev. B* **45**, 7392–7396 (1992).
46. T. Chase, M. Trigo, A. H. Reid, R. Li, T. Vecchione, X. Shen, S. Weathersby, R. Coffee, N. Hartmann, D. A. Reis, X. J. Wang, H. A. Dürr, Ultrafast electron diffraction from non-equilibrium phonons in femtosecond laser heated Au films. *Appl. Phys. Lett.* **108**, 041909 (2016).
47. M. Ligges, I. Rajkovic, P. Zhou, O. Posth, C. Hassel, G. Dumpich, D. von der Linde, Observation of ultrafast lattice heating using time resolved electron diffraction. *Appl. Phys. Lett.* **94**, 101910 (2009).
48. S. Nie, X. Wang, J. Li, R. Clinite, J. Cao, Femtosecond electron diffraction: Direct probe of ultrafast structural dynamics in metal films. *Microsc. Res. Tech.* **72**, 131–143 (2009).
49. J.-A. Yang, S. Parham, D. Dessau, D. Reznik, Novel electron-phonon relaxation pathway in graphite revealed by time-resolved raman scattering and angle-resolved photoemission spectroscopy. *Sci. Rep.* **7**, 40876 (2017).
50. A. F. Kemper, M. A. Sentef, B. Moritz, J. K. Freericks, T. P. Devereaux, Effect of dynamical spectral weight redistribution on effective interactions in time-resolved spectroscopy. *Phys. Rev. B* **90**, 075126 (2014).
51. A. F. Kemper, J. K. Freericks, Relationship between population dynamics and the self-energy in driven non-equilibrium systems. *Entropy* **18**, 180 (2016).
52. B. Renker, F. Gompf, D. Ewert, P. Adelman, H. Schmidt, E. Gering, H. Mutka, Changes in the phonon spectra of Bi 2212 superconductors connected with the metal-semiconductor transition in the series of $\text{Bi}_2\text{Sr}_2(\text{Ca}_{1-x}\text{Y}_x)\text{Cu}_2\text{O}_8$ compounds. *Z. Phys. B Condens. Matter* **77**, 65–68 (1989).
53. W. Zhang, T. Miller, C. L. Smallwood, Y. Yoshida, H. Eisaki, R. A. Kaindl, D.-H. Lee, A. Lanzara, Stimulated emission of Cooper pairs in a high-temperature cuprate superconductor. *Sci. Rep.* **6**, 29100 (2016).
54. Z. Lin, L. V. Zhigilei, V. Celli, Electron-phonon coupling and electron heat capacity of metals under conditions of strong electron-phonon nonequilibrium. *Phys. Rev. B* **77**, 075133 (2008).
55. L. Waldecker, R. Bertoni, R. Ernstorfer, J. Vorberger, Electron-phonon coupling and energy flow in a simple metal beyond the two-temperature approximation. *Phys. Rev. X* **6**, 021003 (2016).
56. Y. Zhu, Q. Li, Y. N. Tsay, M. Suenaga, G. D. Gu, N. Koshizuka, Structural origin of misorientation-independent superconducting behavior at [001] twist boundaries in $\text{Bi}_2\text{Sr}_2\text{CaCu}_2\text{O}_{8+\delta}$. *Phys. Rev. B* **57**, 8601–8608 (1998).
57. S. Kambe, K. Okuyama, S. Ohshima, T. Shimada, Origin of modulated structure for high- T_c Bi2212 superconductor. *Physica C Supercond.* **250**, 50–54 (1995).
58. P. S. Kirchmann, L. Rettig, D. Nandi, U. Lipowski, M. Wolf, U. Bovensiepen, A time-of-flight spectrometer for angle-resolved detection of low energy electrons in two dimensions. *Appl. Phys. A Mater. Sci. Process* **91**, 211–217 (2008).
59. R. Xu, T. C. Chiang, Determination of phonon dispersion relations by x-ray thermal diffuse scattering. *Z. Kristallogr. Cryst. Mater.* **220**, 1009–1016 (2005).
60. Y. Murakami, P. Werner, N. Tsuji, H. Aoki, Interaction quench in the Holstein model: Thermalization crosses from electron- to phonon-dominated relaxation. *Phys. Rev. B* **91**, 045128 (2015).

Acknowledgments: We thank K. Sokolowski-Tinten and G. Coslovich for useful discussions and comments and J. Li for the help with the MeV-UED experiments at the BNL Source Development Laboratory. **Funding:** The MeV-UED work in BNL was supported by the U.S. Department of Energy (DOE), Office of Science, Basic Energy Sciences (BES), Division of Materials Sciences and Engineering (DMSE) under contract no. DESC0012704. The work in Stanford Linear Accelerator Center (SLAC) was supported by the DOE Laboratory Directed Research and Development funding under contract DE-AC02-76SF00515 and by the DOE BES Scientific User Facilities Division and SLAC UED/UEM program development fund under the contract no. DE-AC02-05CH11231. Tr-ARPES work was supported by the Center for Emergent Superconductivity, an Energy Frontier Research Center, headquartered at BNL and funded by the U.S. DOE, under contract no. DE-2009-BNL-PM015 and by the Deutsche Forschungsgemeinschaft through SPP 1458 and SFB 1242 (TP B01). Theory work by J.K.F. was supported by the DOE, Office of BES, DMSE under contract no. DE-FG02-08ER46542 and by the McDevitt bequest at Georgetown. **Author contributions:** Y.Z. conceived and initiated the project, Y.Z. and X.W. coordinated the UED part of the project, and P.D.J. and U.B. coordinated the tr-ARPES part of the project. G.G. and Y.H. prepared the samples.

T.K., A.H.R., R.L., and X.S. performed UED measurements, and T.K. performed the analysis of the UED data with input from Y.Z., L.W., and H.A.D. J.D.R., L.R., I.A., and M.L. performed the tr-ARPES measurements, and J.D.R. performed the analysis of the tr-ARPES data. T.K. and L.W. did the Bloch wave calculations, and O.A., A.F.K., and J.K.F. calculated the growth rate. T.K. and A.F.K. wrote the manuscript with Y.Z. All authors commented on the manuscript.

Competing interests: The authors declare that they have no competing interests. **Data and materials availability:** All data needed to evaluate the conclusions in the paper are present in the paper and/or the Supplementary Materials. Additional data related to this paper may be requested from the authors.

Submitted 23 August 2017

Accepted 12 March 2018

Published 27 April 2018

10.1126/sciadv.aap7427

Citation: T. Konstantinova, J. D. Rameau, A. H. Reid, O. Abdurazakov, L. Wu, R. Li, X. Shen, G. Gu, Y. Huang, L. Rettig, I. Avigo, M. Ligges, J. K. Freericks, A. F. Kemper, H. A. Dürr, U. Bovensiepen, P. D. Johnson, X. Wang, Y. Zhu, Nonequilibrium electron and lattice dynamics of strongly correlated $\text{Bi}_2\text{Sr}_2\text{CaCu}_2\text{O}_{8+\delta}$ single crystals. *Sci. Adv.* **4**, eaap7427 (2018).

Nonequilibrium electron and lattice dynamics of strongly correlated $\text{Bi}_2\text{Sr}_2\text{CaCu}_2\text{O}_{8+\delta}$ single crystals

Tatiana Konstantinova, Jonathan D. Rameau, Alexander H. Reid, Omadillo Abdurazakov, Lijun Wu, Renkai Li, Xiaozhe Shen, Genda Gu, Yuan Huang, Laurenz Rettig, Isabella Avigo, Manuel Ligges, James K. Freericks, Alexander F. Kemper, Hermann A. Dürr, Uwe Bovensiepen, Peter D. Johnson, Xijie Wang and Yimei Zhu

Sci Adv 4 (4), eaap7427.
DOI: 10.1126/sciadv.aap7427

ARTICLE TOOLS

<http://advances.sciencemag.org/content/4/4/eaap7427>

SUPPLEMENTARY MATERIALS

<http://advances.sciencemag.org/content/suppl/2018/04/23/4.4.eaap7427.DC1>

REFERENCES

This article cites 58 articles, 4 of which you can access for free
<http://advances.sciencemag.org/content/4/4/eaap7427#BIBL>

PERMISSIONS

<http://www.sciencemag.org/help/reprints-and-permissions>

Use of this article is subject to the [Terms of Service](#)

Science Advances (ISSN 2375-2548) is published by the American Association for the Advancement of Science, 1200 New York Avenue NW, Washington, DC 20005. The title *Science Advances* is a registered trademark of AAAS.

Copyright © 2018 The Authors, some rights reserved; exclusive licensee American Association for the Advancement of Science. No claim to original U.S. Government Works. Distributed under a Creative Commons Attribution NonCommercial License 4.0 (CC BY-NC).